Desalination and Water Treatment
www.deswater.com

doi: 10.5004/dwt.2021.27201

225 (2021) 320–330
June

Vertical growth of 2D BiOCl nanosheets on FeOCl nanoplates as an efficient photo-Fenton catalyst for phenol degradation

Linlin Jiang[a], Mingkai Gong[a], Xinyu Jiang[a], Jian Zhang[a,*], Guodong Liu[a,*], Qingming Zeng[b,*]

[a]*Department of Chemistry and Chemical Engineering, Jining University, Qufu 273100, P.R. China, Tel. +86-537-3196089; emails: sduchemzhang@163.com (J. Zhang), liugd615@163.com (G. Liu), jll920@126.com (L. Jiang), gmk2019@163.com (M. Gong), 616689286@qq.com (X. Jiang)*

[b]*Shandong Technology Research Center for High Performance Silicone Seal, Weifang 261000, P.R. China, Tel. +86-537-3196089; email: 492656348@qq.com*

Received 13 June 2020; Accepted 3 March 2021

ABSTRACT

The synthesis of the photo-Fenton catalysts with novel structures is of great importance. Herein, a novel strategy is developed for photo-Fenton catalyst via *in-situ* vertical growth of 2D BiOCl nanosheet on FeOCl nanoplate. The BiOCl/FeOCl demonstrates excellent photo-Fenton catalytic performance under simulated sunlight for phenol degradation. The catalytic activity of the BiOCl/FeOCl is five times higher than that of FeOCl. The novel interface structure of –Fe–Cl–Bi– accelerates the electron transfer and increases the structural stability of BiOCl/FeOCl. The photogenerated electrons of BiOCl can reduce the Fe^{3+} to Fe^{2+} ions, which boosts the production of $^{\bullet}OH$ radicals. The results will expand the synthetic pathway of the Fenton catalyst with a novel interfacial structure.

Keyworks: FeOCl; BiOCl; Photo-Fenton; Nanosheets; Phenol

1. Introduction

Nowadays, advanced oxidation technologies have become an effective way to solve the environmental crisis [1,2]. Among them, the photo-Fenton catalytic technology has attracted much attention [3–5]. Iron-based compounds are usually used as photo-Fenton catalysts. The photogenerated electrons in the photo-Fenton catalysis can reduce Fe^{3+} to Fe^{2+}, which promotes the generation of $^{\bullet}OH$ radical [4]. Therefore, the accelerated charge separation of iron-based compounds is the key to improve the photo-Fenton catalytic performance.

Recently, ElShafei et al. [6] have shown that the metal oxychlorides have good catalytic activity as robust heterogeneous Fenton catalysts [7]. The FeOCl shows the best Fenton catalytic activity among metal oxychlorides under UV light [6]. BiOCl has been studied as a photo-Fenton catalyst based on the oxygen vacancy of electron-donor nature [8]. The doping of Fe^{3+} in BiOCl can increase the photo-Fenton catalytic activity under visible light [9–13]. Moreover, the FeOCl also shows the best Fenton catalytic activity than other iron oxides [14]. However, owing to the small bandgap of FeOCl (about 1.8 eV), the recombination rate of the photogenerated electron–hole pair is very high [15]. The combination of FeOCl and photocatalyst with a similar crystal structure appears to be an effective method. Therefore, it is reasonable to expect that the BiOCl modified FeOCl will be a novel photo-Fenton catalyst with excellent catalytic activity.

Based on the above analysis, BiOCl/FeOCl has been successfully prepared as an efficient photo-Fenton catalyst for phenol degradation. The 2D BiOCl nanosheet anchored on FeOCl nanoplate surface. The accelerated charge transfer

* Corresponding authors.

of the BiOCl/FeOCl has been evidenced by measuring the yield of •OH radical. The photo-Fenton catalytic activity of the BiOCl/FeOCl is five times higher than that of FeOCl. The cycle number of BiOCl/FeOCl increased to five. This work will help to provide a reasonable strategy for the preparation of novel FeOCl based photo-Fenton catalysts.

2. Experimental

2.1. Synthesis of BiOCl/FeOCl

All the chemicals with analytical grade (Sinopharm Chemical Reagent Co., Ltd., China) are used in our experiments. The pure FeOCl was synthesized by calcining $FeCl_3 \cdot 6H_2O$ at 230°C for 1 h. 0.05 g pure FeOCl was dispersed in 10 mL H_2O with ultrasound for 5 min at 25°C. 20 mL $Bi(NO_3)_3$ aqueous solution (2 M) was added to the above suspension and stirred strongly for 2 h. After washing three times, the product dried at 90°C in a vacuum oven for 12 h and named as BiOCl/FeOCl-2. The BiOCl/FeOCl-1 and BiOCl/FeOCl-3 were prepared by adding 0.02 mol and 0.06 mol $Bi(NO_3)_3$, respectively.

2.2. Catalytic tests

The 100 mL suspension with 50 mg BiOCl/FeOCl and 0.5 mg phenol were stirred for 60 min in the dark. Start the timer after adding 0.8 mL H_2O_2 (30 weight%) and turning on the simulated sunlight. 5 mL of suspension was taken out every 2 min to detect the UV-vis absorption spectra. The scavengers (1 mM) were used to detect the active species, which were benzoquinone (BQ), ammonium oxalate (AO), and iso-propyle alcohol (IPA) [16,17]. The decomposition of H_2O_2 was detected by fluorescence technique. The test method is the same as the above catalytic test except that the terephthalic acid is added as a trapping agent [18,19].

2.3. Characterization

The crystalline phase of the sample was measured by X-ray diffraction (XRD; Rigaku D/Max 2200-PC). The morphology was characterized by scanning electron microscopy (SEM; ZEISS system). The fine structure was further measured by transmission electron microscopy (TEM; JEM-100CXII). The detailed structure of the sample was studied by the Fourier transform infrared (FTIR; Nicolet 5DX) spectra. The elements of the sample were measured by the X-ray photoelectron spectra (XPS; PerkinElmer PHI-5300 ESCA). The optical adsorption was collected by UV/vis spectrophotometer (Lambda-35, PerkinElmer). QuadraSorb SI was used to collect the information of the surface area and pore distribution. The H_2O_2 decomposition was studied by an F-4600 fluorescence spectrophotometer. Inductively coupled plasma mass spectrometry (ICP-MS) was used to measure the leaching of Bi and Fe on Nu ATTOM measurements.

3. Results and discussion

3.1. Catalyst characterization

Fig. 1a shows the schematic diagram of the synthesis process of BiOCl/FeOCl. The FeOCl nanoplates are prepared by a simple one-step low-temperature calcination method. The Bi^{3+} in the solution reacted with FeOCl *in-situ* to form two-dimension (2D) BiOCl nanosheets at 25°C, which were anchored on FeOCl nanoplates surface. The $[Bi_2O_2]^{2+}$ was first bonded with Cl^- on FeOCl surface to form a –O–Fe–Cl–Bi–O– interface. Using Cl as a bridge, a stable interface structure was formed between the BiOCl and FeOCl. To characterize the crystal structure of the samples, XRD measurement is carried out (Fig. 1b), which shows that the pure FeOCl is orthorhombic (JCPDS, No. 24-1005). When a small amount of $Bi(NO_3)_3$ is added, most of the diffraction peaks of BiOCl/FeOCl-1 are the same as those of the pristine FeOCl. However, the new diffraction peaks of BiOCl/FeOCl-1 at 32.8° and 33.4° are attributed to the (110) and (102) of BiOCl, respectively [20]. The fact indicates that the BiOCl has been successfully combined with FeOCl. As for the BiOCl/FeOCl-2, a new diffraction peak appears at 24.1°, which is related to the (002) of BiOCl [21]. No peaks of other phases are detected. In the XRD pattern of BiOCl/FeOCl-3, the impurities are observed, indicating that excessive $Bi(NO_3)_3$ leads to other products. Fig. 1c is the SEM image of the BiOCl/FeOCl-2, the BiOCl nanosheets are vertically fixed on the FeOCl surface. TEM is further measured to study the novel morphology of the BiOCl/FeOCl-2 (Fig. 1d), which shows that the BiOCl has grown on the surface of FeOCl. The low contrast of BiOCl implies the characteristics of nanosheet structure [22,23]. To further confirm the BiOCl, the high-resolution transmission electron microscopy image (HRTEM) is also carried out (Fig. 1e), which demonstrates that the lattice fringes are observed with a lattice spacing of 0.74 and 0.28 nm, corresponding to the (001) and (110) crystal plane of BiOCl, respectively [24,25]. The energy-dispersive X-ray spectroscopy (EDS) results indicate that all the elements of Fe, Bi, O, and Cl are detected (Fig. 1f). The corresponding mapping images in Figs. 1g–j show that the Fe, Bi, O, and Cl are uniformly dispersed in the BiOCl/FeOCl-2. The close contact between FeOCl and BiOCl is propitious to strengthen the contact between them and promote the rapid charge transfer at the interface.

The morphology was characterized by the SEM measurements (Fig. 2). The morphology of the pure FeOCl is nanoplate with a thickness of about 300 nm (Fig. 2a). The surface of pure FeOCl is smooth. However, the surface of FeOCl nanoplates in BiOCl/FeOCl-2 is covered with vertically grown BiOCl nanosheets. The thickness of the BiOCl nanosheet is ca.10 nm (Fig. 2b). In the case of BiOCl/FeOCl-1 (Fig. 2c), only a small amount of BiOCl adhered to the surface of FeOCl, which is due to the small additional amount of $Bi(NO_3)_3$. As for the BiOCl/FeOCl-3 (Fig. 2d), a large number of bismuth compounds are dispersed around the FeOCl.

In order to study the detailed composite structure of the BiOCl/FeOCl, FTIR spectrums are measured as seen in Fig. 3a. The peaks in the range of 3,000–3,700 cm^{-1} are assigned to the stretching vibration of hydroxyl groups in pure FeOCl. The peak at 490 cm^{-1} is attributed to Fe–O stretching [26,27]. The adsorbed water on the FeOCl surface is at 1,620 cm^{-1} [28,29]. In the FTIR spectrums of the BiOCl/FeOCl, the peak at 1,380 cm^{-1} belongs to nitrate [30]. Compared with pure FeOCl, the peak intensity of hydroxyl groups in BiOCl/FeOCl is obviously weakened. It indicates a relatively small OH bonding group in BiOCl/FeOCl. Owing to the weak bonding strength of Cl on the FeOCl

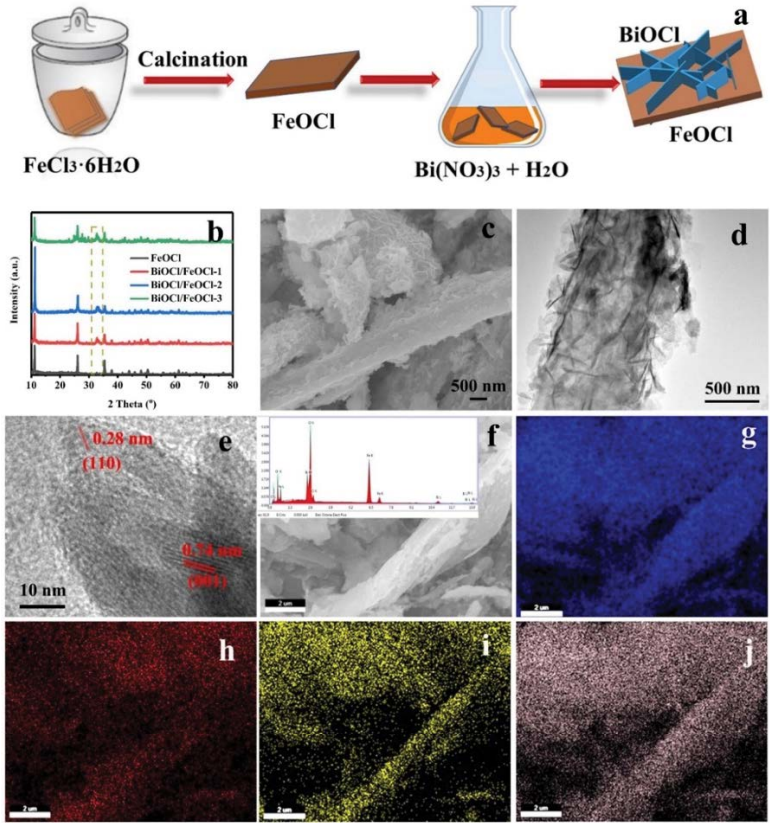

Fig. 1. (a) Schematic diagram of the synthesis process of BiOCl/FeOCl nanosheets, (b) XRD patterns of BiOCl/FeOCl, (c) SEM image, (d) TEM image, (e) HRTEM image, (f) EDS of BiOCl/FeOCl-2, elemental mapping images of BiOCl/FeOCl-2 with (g) Fe, (h) Bi, (i) O, and (j) Cl.

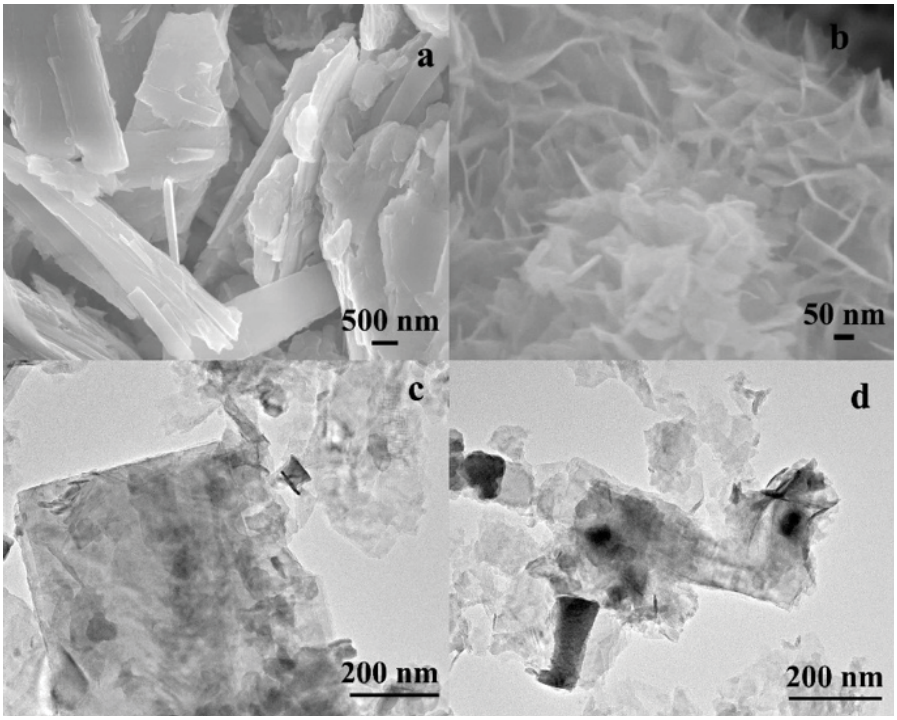

Fig. 2. SEM images of (a) pure FeOCl and (b) BiOCl/FeOCl-2, TEM images of the (c) BiOCl/FeOCl-1 and (d) BiOCl/FeOCl-3.

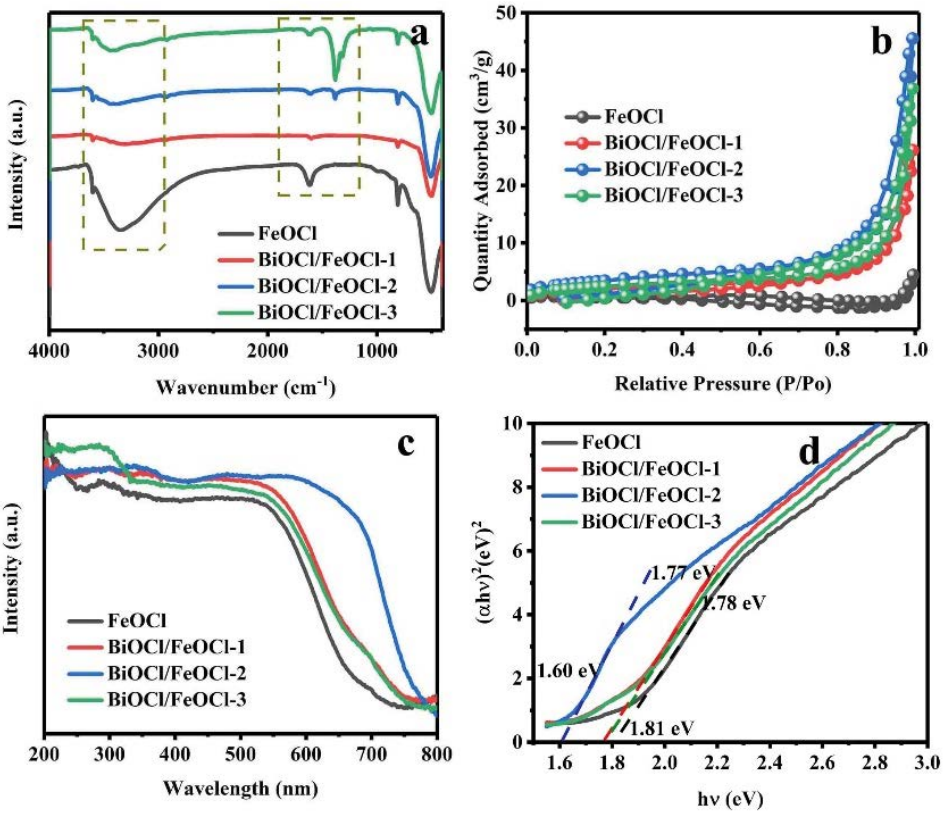

Fig. 3. (a) FTIR spectrums, (b) N_2 adsorption–desorption isotherms, (c) ultraviolet-visible diffusive reflectance spectra, and (d) the bandgap value of FeOCl, BiOCl/FeOCl-1, BiOCl/FeOCl-2, and BiOCl/FeOCl-3.

surface, the OH group can replace part of the chloride on the FeOCl surface in solution, resulting in poor structure stability of pure FeOCl. The weak bonding of the OH group in BiOCl/FeOCl implies the increased structural stability in the solution, which is propitious to improve catalytic performance.

The yield of hydroxyl radical in Fenton catalysis is a key index to evaluate the performance of the catalyst. The high specific surface of the Fenton catalyst not only has a large number of active sites but also means increased contact with H_2O_2 to generate hydroxyl radical. Thus, the surface area of the prepared sample is measured by the N_2 adsorption–desorption isotherms as seen in Fig. 3b. The surface area of the pure FeOCl is 1.6 m^2/g, and that of the BiOCl/FeOCl-1 is 7.7 m^2/g. The surface area of the BiOCl/FeOCl-2 is the highest (13.0 m^2/g). The surface area of the BiOCl/FeOCl-3 decreases to 9.4 m^2/g. The corresponding pore volumes of pure FeOCl, BiOCl/FeOCl-1, BiOCl/FeOCl-2, and BiOCl/FeOCl-3 are 0.004, 0.035, 0.070, and 0.057 m^3/g, respectively.

The optical properties of the samples are characterized by UV-vis reflectance spectra, which are displayed in Fig. 3c. The absorption edge band of the BiOCl/FeOCl obviously moves to the direction of high absorption. Among them, the redshift of the BiOCl/FeOCl-2 is the largest. The BiOCl/FeOCl-2 has a wide absorption tag of 300–800 nm, indicating that the BiOCl/FeOCl-2 possesses excellent solar light utilization efficiency. According to the literature [31], the calculated optical band gap value of the pure FeOCl is 1.81 eV (Fig. S1). After doping with BiOCl, the bandgap values of the BiOCl/FeOCl-1, BiOCl/FeOCl-2, and BiOCl/FeOCl-3 decreased to 1.77, 1.60, and 1.78 eV (Fig. 3d), respectively. On the one hand, this result shows that the modification of BiOCl can change the bandgap of FeOCl. On the other hand, the results also imply that the BiOCl/FeOCl-2 could have excellent photo-Fenton catalytic performance under sunlight.

XPS measurements are further carried out to study the chemical state of the samples. The XPS spectra of the BiOCl/FeOCl-2 in Fig. S2a show the strong signals of Fe, Bi, O, and Cl elements, indicating the successful combination of them. Fig. 4a is the Fe 2p XPS spectrum of BiOCl/FeOCl-2, which shows that the peaks at 710.1 and 723.4 eV are assigned to the Fe 2p3/2 and Fe 2p1/2 peak, respectively. Combined with the peak at 717.3 eV, the Fe in the BiOCl/FeOCl-2 is determined as Fe^{3+} state [32]. However, the characteristic peaks of Fe 2p in pure FeOCl are at 710.7 and 724.0 eV, which shift to a small angle (0.6 eV) compared with that in BiOCl/FeOCl-2, indicating the partial reduction of Fe^{3+} in the BiOCl/FeOCl-2. Owing to the chemical bonding between –Bi–Cl– and FeOCl surface, the chemical bond strength of Fe–Cl decreases, which results in the partial reduction of Fe^{3+} in the BiOCl/FeOCl-2. The fact also further proves the formed novel interface structure of –Fe–Cl–Bi– in the BiOCl/FeOCl-2. Furthermore, the comparison of the Bi 4f XPS spectrums between BiOCl/FeOCl-2

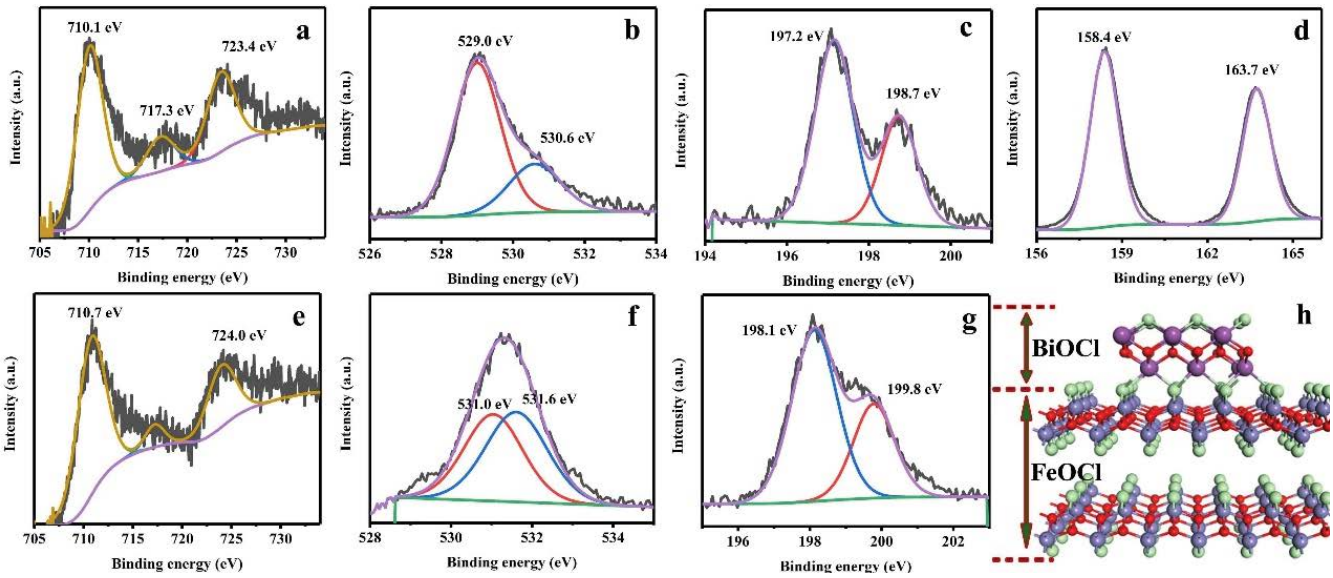

Fig. 4. XPS spectrums of (a) Fe 2p, (b) O 1s, (c) Cl 2p, and (d) Bi 4f in BiOCl/FeOCl-2, (e) Fe 2p, (f) O 1s, and (g) Cl 2p in pure FeOCl, (h) the schematic representation of the BiOCl/FeOCl-2.

and BiOCl/FeOCl-3 can also prove this viewpoint. The two peaks are at 163.7 and 158.4 eV, corresponding to Bi 4f7/2 and Bi 4f5/2 of Bi^{3+} (Fig. 4d), respectively [9,10]. However, the characteristic peaks of Bi^{3+} shift to 163.9 and 158.6 eV in the BiOCl/FeOCl-3 (Fig. S2b). For the same reason, the binding energies of Bi^{3+} in BiOCl/FeOCl-2 are smaller than those in BiOCl/FeOCl-3.

The O1s XPS spectra of the BiOCl/FeOCl-2 in Fig. 4b show two peaks at 529.0 and 530.6 eV, which are ascribed to the crystal lattice oxygen and hydroxyl oxygen, respectively [33,34]. Whereas the peaks of O1s in pure FeOCl in Fig. 4f are at 531.0 and 531.6 eV. Compared with pure FeOCl, the content of hydroxyl oxygen decreases, which consists of the FTIR results (Fig. 3a). The increased content of crystal lattice oxygen in BiOCl/FeOCl-2 indicates the existing Bi–O in the composite. Meanwhile, compared with pure FeOCl, the shifted peaks of O1s in the BiOCl/FeOCl-2 further prove the existent interaction between FeOCl and BiOCl. The Cl 2p XPS spectrum shows two peaks with binding energies at 197.2 and 198.7 eV, corresponding to Cl 2p3/2 and Cl 2p1/2 of Cl^- (Fig. 4c), respectively [11,12]. The peaks of Cl 2p in pure FeOCl locate at 198.1 and 199.8 eV (Fig. 4g). The obvious shift peaks of Cl 2p in the BiOCl/FeOCl-2 are caused by the interface structure, which further proves the existence of a covalent chemical bond between BiOCl and FeOCl.

Therefore, based on the above structural characterization results, the 2D BiOCl nanosheets have been successfully vertically anchored to the FeOCl surface by using Cl as a bridge at the interface (Fig. 4h). The bigger surface area of the BiOCl/FeOCl-2 can provide a large number of active sites. The BiOCl/FeOCl-2 should have an excellent photo-response under sunlight. Meanwhile, the novel interface structure will facilitate the accelerated charge transfer at the interface.

It is expected that an efficient photo-Fenton catalyst will be obtained. Thus, using phenol as a degradation agent, the photo-Fenton catalytic performance of the samples was measured in neutral solution (pH = 7) and simulated sunlight. Fig. 5a is the photo-Fenton catalytic activities of the prepared samples. It is clearly observed that all the BiOCl/FeOCl exhibit excellent photo-Fenton catalytic activity for phenol degradation, while pure FeOCl displays a relatively low activity. It indicates that the photo-Fenton catalytic activity of FeOCl improves by the introduction of BiOCl. The BiOCl/FeOCl-2 has the highest catalytic activity within 12 min. The corresponding kinetic plots of these samples are also depicted in Fig. 5b. The degradation constants (k) of the FeOCl, BiOCl/FeOCl-1, BiOCl/FeOCl-2, and BiOCl/FeOCl-3 are 0.06, 0.07, 0.32, and 0.10 min^{-1}, respectively. The photo-Fenton catalytic activity of the BiOCl/FeOCl-2 is five times higher than that of pure FeOCl.

Fig. 5c shows the degradation efficiency of the BiOCl/FeOCl-2 under different experimental conditions. It shows that the catalytic activity of the BiOCl/FeOCl-2 is low under dark (19%), while it increases to 85% after adding H_2O_2. It is worth mentioning that the photocatalytic activity of the BiOCl/FeOCl-2 is low. It can be seen that the Fenton catalytic activity of the BiOCl/FeOCl-2 in the dark is obviously better than the photocatalytic activity of the BiOCl/FeOCl-2. Therefore, although the excellent catalytic activity of the BiOCl/FeOCl-2 is derived from the contribution of Fenton catalysis and photocatalysis, the Fenton catalysis plays a more important role. In addition, the decreased amount of phenol on the BiOCl/FeOCl-2 in the dark (19%, Fig. 5c) is mainly due to the surface adsorption caused by the high surface area of the BiOCl/FeOCl-2 (Fig. 3b). Owing to the key role of H_2O_2, the effect of the H_2O_2 content on the photo-Fenton catalytic activity of the BiOCl/FeOCl-2 was also measured (Fig. 5d). It shows that the degradation efficiency improves with the addition of 8.5 mmol H_2O_2, and further increases with the addition of 27.2 mol H_2O_2. However, the degradation efficiency

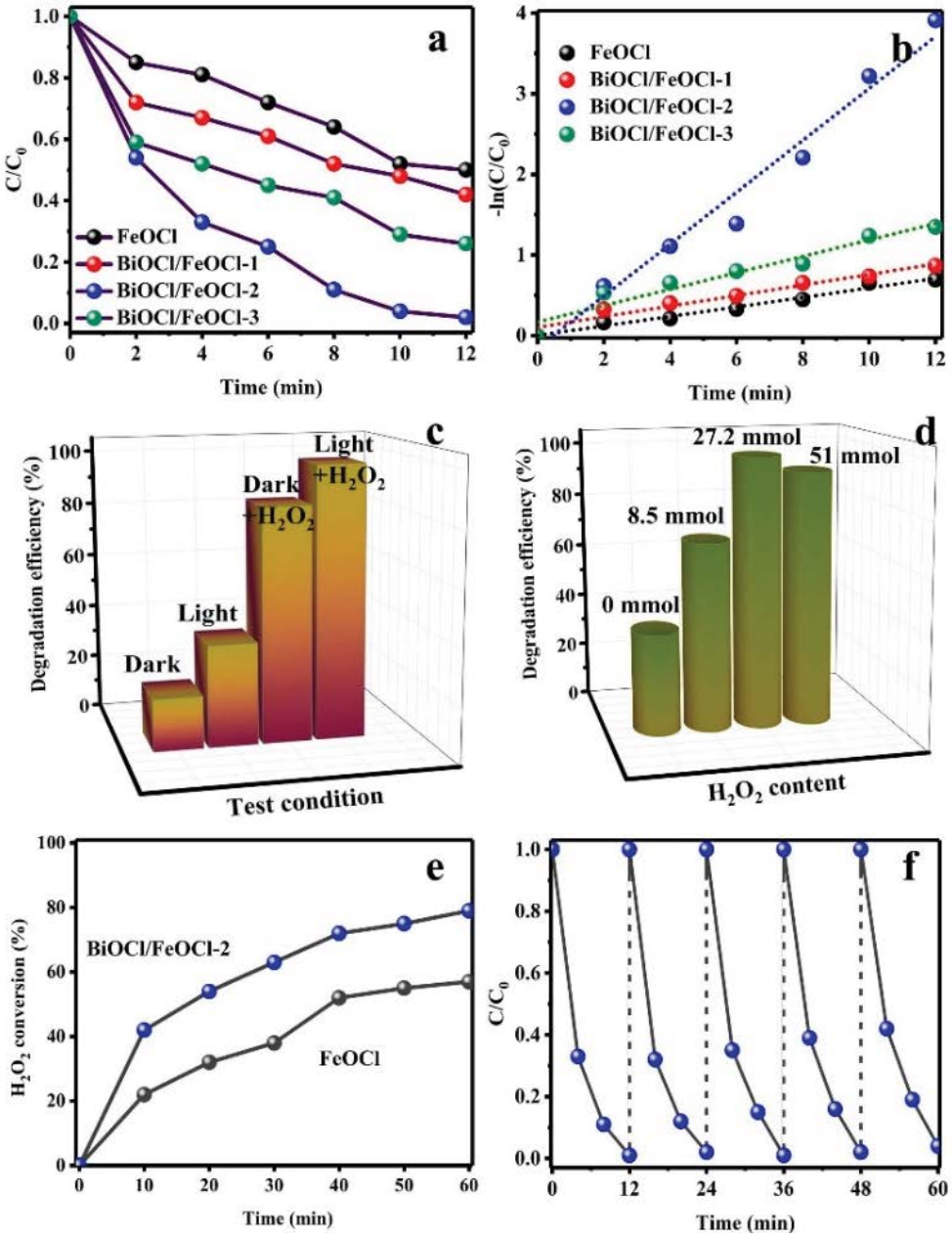

Fig. 5. (a) Photo-Fenton catalytic activity and (b) the corresponding kinetic plots over FeOCl, BiOCl/FeOCl-1, BiOCl/FeOCl-2, and BiOCl/FeOCl-3, (c) degradation efficiency of BiOCl/FeOCl-2 by different (c) test conditions and (d) H_2O_2 content, (e) H_2O_2 conversion over FeOCl and BiOCl/FeOCl-2, (f) cycling experiments of BiOCl/FeOCl-2.

decreases when the addition amount of H_2O_2 reaches 51 mol. Owing to the limited number of catalytic active sites in the BiOCl/FeOCl-2, a small amount of H_2O_2 means more attachment between H_2O_2 and the active sites. But excessive H_2O_2 cannot react with H_2O_2 sufficiently. Besides, the generated $^{\bullet}OH$ radical can also be partially consumed by excessive H_2O_2 [35,36]. The pH value in the photo-Fenton system can affect the degradation performance of pollutants, thus the effect of pH value on phenol degradation was also investigated (Fig. S3). It indicates that the degradation activity of BiOCl/FeOCl-2 decreased with the increase of pH value. The catalytic activity in acidic solution is higher than that in alkaline solution.

In photo-Fenton catalysis, the $^{\bullet}OH$ radical is the most important active species. Therefore, using the terephthalic acid as a trapping agent, the decomposition of H_2O_2 is determined by fluorescence technique as seen in Fig. 5e, which shows that the conversion of H_2O_2 over the BiOCl/FeOCl-2 is obviously better than that over pure FeOCl. Thus, the presence of BiOCl in the composite effectively accelerates the decomposition of H_2O_2 to produce $^{\bullet}OH$ radicals. Further cycling experiments are carried out to measure

the recycling performance of the BiOCl/FeOCl-2 as seen in Fig. 5f, which demonstrates that the BiOCl/FeOCl-2 maintains high photo-Fenton catalytic activity in five cycles. Whereas, the pure FeOCl can only maintain its catalytic activity in two cycles (Fig. S4). It indicates that the BiOCl/FeOCl-2 shows higher structural stability than pure FeOCl, which consists of the above structural characterization results. The interface bonding of –Fe–Cl–Bi– effectively prevents the loss of chloride ions on the FeOCl surface and improves the stability of the structure. Furthermore, the structural characterization of the BiOCl/FeOCl-2 after photo-Fenton catalysis reaction is also carried out (Fig. S5). The TEM image of the BiOCl/FeOCl-2 demonstrates the well-preserved morphology (Fig. S5a). The XPS spectrum of the BiOCl/FeOCl-2 shows the stability of the chemical state and composition (Fig. S5b). Moreover, to avoid the secondary pollution to water, the leaching amounts of Fe and Bi are also measured by the ICP-MS. The results reveal that the leaching amounts of Fe and Bi are 0.71 and 0.03 ppm, respectively, which are very small and would not cause secondary pollution [14].

In order to study the catalytic mechanism, the active species are detected by the trapping experiments as seen in Fig. 6, which has been proved to be an effective way by Fan et al. [37,38]. Moreover, the suppressed degradation degree can also represent the content of active species [39–41]. Fig. 6a shows the degradation efficiency of the BiOCl/FeOCl-2 by introducing scavenger into the photo-Fenton catalysis. The IPA causes the biggest suppressed degradation efficiency, which suggests that the •OH radical plays the most important role in these active species. And the amount of the •OH radical in the reaction system is also the biggest, which comes from the decomposition of H_2O_2. Using BQ as a scavenger, the role of superoxide radical is studied, which also plays an important role in photo-Fenton catalysis. However, the contribution of photogenerated holes detected by introducing AO is small (Fig. 6a).

Fig. 6b is the trapping experiment over BiOCl/FeOCl-2 in the dark. The BiOCl cannot excite photogenerated electrons and holes in the dark. Thus, compared with the trapping experiment under simulated sunlight, the production of superoxide radicals obviously reduced. It indicates that the superoxide radicals mainly come from the reaction of dissolved oxygen and photogenerated electrons, which is from the BiOCl in the composite. According to the literature, the conduction band of FeOCl is 0.98 eV, which is more positive than the potential of $O_2/{}^{\bullet}O^{2-}$ [42]. The conduction band of BiOCl is –1.09 eV, which is more negative than the potential of $O_2/{}^{\bullet}O^{2-}$ [43]. Therefore, the generated ${}^{\bullet}O^{2-}$ radicals are from the reaction between photogenerated electrons and dissolved oxygen [44,45]. Fig. 6b also shows that the production of •OH radical is bigger than that of superoxide radical. The fact suggests that the FeOCl in the composite mainly decomposes H_2O_2 to generates •OH radical, while BiOCl in the composite mainly produces superoxide radicals. Furthermore, the suppressed degradation efficiency of the BiOCl/FeOCl-2 by IPA under simulated sunlight is significantly bigger than that under dark, implying that the simulated sunlight also promotes the production of •OH radical. The photogenerated electrons in BiOCl are captured by Fe^{3+} in FeOCl through the interface bonding, which accelerates the reduction of Fe^{3+} to Fe^{2+} and promotes the generation of •OH radical, in accordance with the literatures [9,10].

In this study, the novel composite structure of 2D BiOCl nanosheets vertically anchored on FeOCl nanoplates greatly improved the photo-Fenton catalytic activity. Based on the above experimental results, the photo-Fenton catalytic process under simulated sunlight irradiation is illustrated in Fig. 7. Under simulated sunlight, owing to the ultrathin nanosheet structure and self-induced internal electric field of BiOCl, the photogenerated electrons and holes are easily separated [46,47]. Partial photogenerated electrons transfer to the BiOCl surface and react with dissolved oxygen to form superoxide radicals [48,49]. At the same time, some of the photogenerated electron transfer to FeOCl through the –Fe–Cl–Bi– interface, resulting in the reduction of Fe^{3+} to Fe^{2+} ions. The transferred photogenerated electrons enhanced the separation ability of photo-generated charge carriers and increased the electrons that participated in the Fe^{2+}/Fe^{3+} cycle [50–52]. The Fe^{2+} ions accelerate the formation of •OH radical from H_2O_2. Furthermore, the high

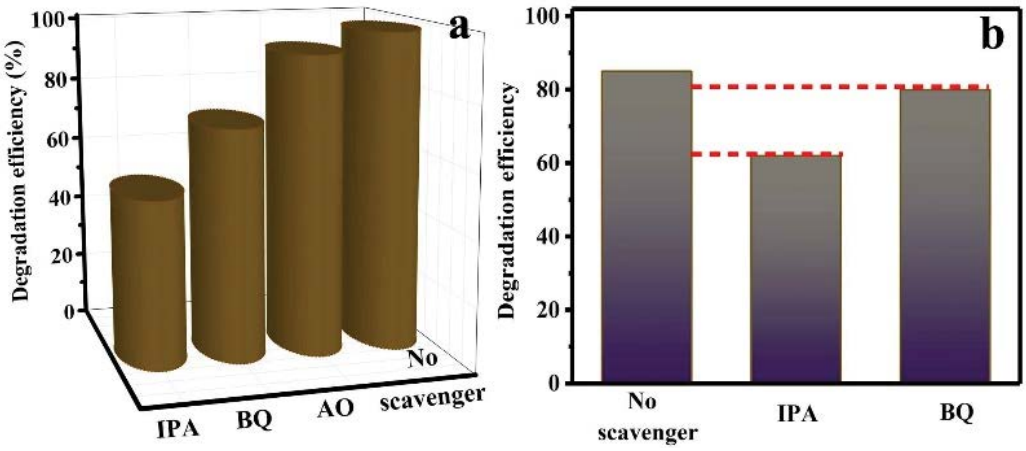

Fig. 6. Trapping experiment of active species over BiOCl/FeOCl-2 under (a) simulated sunlight and (b) dark.

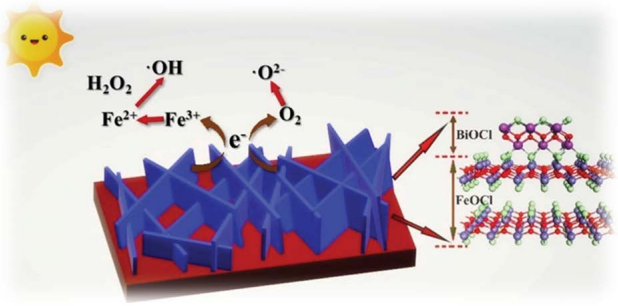

Fig. 7. Schematic diagram of the mechanism for the enhanced photo-Fenton catalytic performance of the BiOCl/FeOCl-2.

surface area of BiOCl/FeOCl-2 increases the adsorption of hydrogen peroxide and phenol on its surface, which effectively improves the contact between phenol and active species, promoting the degradation of phenol.

4. Conclusion

In summary, the 2D BiOCl nanosheets vertically anchored on FeOCl nanoplates are successfully fabricated by an *in-situ* synthesis method. The BiOCl/FeOCl-2 effectively increased the surface area and the utilization of sunlight. The formed novel structure and nanosheet morphology promote interfacial charge transfer. The novel structure of the BiOCl/FeOCl-2 boosts the surface Fenton reaction. The BiOCl/FeOCl-2 presents a five times acceleration of photo-Fenton catalytic degradation rate for phenol. Furthermore, the interface bonding of –Fe–Cl–Bi– effectively prevents the loss of Cl on the FeOCl surface and improve the stability and durability of the composite. The synthesis of the BiOCl/FeOCl provides a new research idea for the preparation of Fenton catalysts.

Acknowledgments

This work was financially supported by the Natural Science Foundation of China (Grant No. 21971086), Natural Science Foundation of Shandong Province (ZR2019MB013), and Young Innovative Talents Introduction and Cultivation Program for Colleges and Universities of Shandong Province: Innovative Research Team on Optoelectronic Functional Materials.

References

[1] X. Duan, H. Sun, S. Wang, Metal-free carbocatalysis in advanced oxidation reactions, Acc. Chem. Res., 51 (2018) 678–687.
[2] A.R. Lado Ribeiro, N.F.F. Moreira, G. Li Puma, A.M.T. Silva, Impact of water matrix on the removal of micropollutants by advanced oxidation technologies, Chem. Eng. J., 363 (2019) 155–173.
[3] Y. Zhu, R. Zhu, Y. Xi, J. Zhu, G. Zhu, H. He, Strategies for enhancing the heterogeneous Fenton catalytic reactivity: a review, Appl. Catal., B, 255 (2019) 117739, doi: 10.1016/j.apcatb.2019.05.041.
[4] A.V. Vorontsov, Advancing Fenton and photo-Fenton water treatment through the catalyst design, J. Hazard. Mater., 372 (2019) 103–112.
[5] E. Brillas, S. Garcia-Segura, Benchmarking recent advances and innovative technology approaches of Fenton, photo-Fenton, electro-Fenton, and related processes: a review on the relevance of phenol as model molecule, Sep. Purif. Technol., 237 (2020) 116337, doi: 10.1016/j.seppur.2019.116337.
[6] G.M.S. ElShafei, A.M. Al-Sabagh, F.Z. Yehia, C.A. Philip, N.A. Moussa, G. Eshaq, A.E. ElMetwally, Metal oxychlorides as robust heterogeneous Fenton catalysts for the sonophotocatalytic degradation of 2-nitrophenol, Appl. Catal., B, 224 (2018) 681–691.
[7] A.E. ElMetwally, G. Eshaq, A.M. Al-Sabagh, F.Z. Yehia, C.A. Philip, N.A. Moussa, G.M.S. ElShafei, Insight into heterogeneous Fenton-sonophotocatalytic degradation of nitrobenzene using metal oxychlorides, Sep. Purif. Technol., 210 (2019) 452–462.
[8] H. Li, J. Shang, Z. Yang, W. Shen, Z. Ai, L. Zhang, Oxygen vacancy associated surface Fenton chemistry: surface structure dependent hydroxyl radicals generation and substrate dependent reactivity, Environ. Sci. Technol., 51 (2017) 5685–5694.
[9] X. Zhong, K.-X. Zhang, D. Wu, X.-Y. Ye, W. Huang, B.-X. Zhou, Enhanced photocatalytic degradation of levofloxacin by Fe-doped BiOCl nanosheets under LED light irradiation, Chem. Eng. J., 383 (2020) 123148, doi: 10.1016/j.cej.2019.123148.
[10] F. Tian, G. Li, H. Zhao, F. Chen, M. Li, Y. Liu, R. Chen, Residual Fe enhances the activity of BiOCl hierarchical nanostructure for hydrogen peroxide activation, J. Catal., 370 (2019) 265–273.
[11] M. Gao, D. Zhang, X. Pu, H. Li, W. Li, X. Shao, D. Lv, B. Zhang, J. Dou, Combustion synthesis of Fe-doped BiOCl with high visible-light photocatalytic activities, Sep. Purif. Technol., 162 (2016) 114–119.
[12] Y. Mi, L. Wen, Z. Wang, D. Cao, R. Xu, Y. Fang, Y. Zhou, Y. Lei, Fe(III) modified BiOCl ultrathin nanosheet towards high-efficient visible-light photocatalyst, Nano Energy, 30 (2016) 109–117.
[13] J. Xia, L. Xu, J. Zhang, S. Yin, H. Li, H. Xu, J. Di, Improved visible light photocatalytic properties of Fe/BiOCl microspheres synthesized via self-doped reactable ionic liquids, CrystEngComm, 15 (2013) 10132–10141.
[14] X.-j. Yang, X.-m. Xu, J. Xu, Y.-f. Han, Iron oxychloride (FeOCl): an efficient Fenton-like catalyst for producing hydroxyl radicals in degradation of organic contaminants, J. Am. Chem. Soc., 135 (2013) 16058–16061.
[15] J. Zhang, M. Zhan, L. Zheng, C. Zhang, G. Liu, J. Sha, S. Liu, S. Tian, FeOCl/POM heterojunctions with excellent Fenton catalytic performance via different mechanisms, Inorg. Chem., 58 (2019) 250–258.
[16] Y. Wu, H. Wang, W. Tu, Y. Liu, Y.Z. Tan, X. Yuan, J.W. Chew, Quasi-polymeric construction of stable perovskite-type $LaFeO_3$/g-C_3N_4 heterostructured photocatalyst for improved Z-scheme photocatalytic activity via solid p-n heterojunction interfacial effect, J. Hazard. Mater., 347 (2018) 412–422.
[17] J. Zhang, Q. Liu, H. He, F. Shi, G. Huang, B. Xing, J. Jia, C. Zhang, Coal tar pitch as natural carbon quantum dots decorated on TiO_2 for visible light photodegradation of rhodamine B, Carbon, 152 (2019) 284–294.
[18] J. Chen, Y. Si, Y. Liu, S. Wang, S. Wang, Y. Zhang, B. Yang, Z. Zhang, S. Zhang, Starch-regulated copper-terephthalic acid as a pH/hydrogen peroxide simultaneous-responsive fluorescent probe for lysosome imaging, Dalton Trans., 48 (2019) 13017–13025.
[19] X. Liu, C. Wang, T. Zhu, Q. Lv, Y. Li, D. Che, Simultaneous removal of NO_x and SO_2 from coal-fired flue gas based on the catalytic decomposition of H_2O_2 over $Fe_2(MoO_4)_3$, Chem. Eng. J., 371 (2019) 486–499.
[20] J. Zhong, Y. Zhao, L. Ding, H. Ji, W. Ma, C. Chen, J. Zhao, Opposite photocatalytic oxidation behaviors of BiOCl and TiO_2: direct hole transfer vs. indirect OH oxidation, Appl. Catal., B, 241 (2019) 514–520.
[21] M. Li, S. Yu, H. Huang, X. Li, Y. Feng, C. Wang, Y. Wang, T. Ma, L. Guo, Y. Zhang, Unprecedented eighteen-faceted BiOCl with a ternary facet junction boosting cascade charge flow and photo-redox, Angew. Chem. Int. Ed., 58 (2019) 9517–9521.

[22] S. Kim, H. Wang, Y.M. Lee, 2D nanosheets and their composite membranes for water, gas, and ion separation, Angew. Chem. Int. Ed., 58 (2019) 17512–17527.
[23] X. Xu, R. Zhao, B. Chen, L. Wu, C. Zou, W. Ai, H. Zhang, W. Huang, T. Yu, Progressively exposing active facets of 2D nanosheets toward enhanced pseudo-capacitive response and high-rate sodium storage, Adv. Mater., 31 (2019) 1900526, doi: 10.1002/adma.201900526.
[24] A. Dandapat, H. Gnayem, Y. Sasson, The fabrication of $BiOCl_xBr_{1-x}$/alumina composite films with highly exposed {001} facets and their superior photocatalytic activities, Chem. Commun., 52 (2016) 2161–2164.
[25] W. Liu, Y. Shang, A. Zhu, P. Tan, Y. Liu, L. Qiao, D. Chu, X. Xiong, J. Pan, Enhanced performance of doped BiOCl nanoplates for photocatalysis: understanding from doping insight into improved spatial carrier separation, J. Mater. Chem. A, 5 (2017) 12542–12549.
[26] T. Yu, R. Yang, X. Zhao, X. Shen, Polyaniline-intercalated FeOCl cathode material for chloride-ion batteries, ChemElectroChem, 6 (2019) 1761–1767.
[27] R. Yang, T. Yu, X. Zhao, Polypyrrole-coated iron oxychloride cathode material with improved cycling stability for chloride ion batteries, J. Alloys Compd., 788 (2019) 407–412.
[28] X.-j. Yang, P.-f. Tian, X.-m. Zhang, X. Yu, T. Wu, J. Xu, Y.-f. Han, The generation of hydroxyl radicals by hydrogen peroxide decomposition on FeOCl/SBA-15 catalysts for phenol degradation, AIChE J., 61 (2015) 166–176.
[29] W.-K. Wang, J.-J. Chen, M. Gao, Y.-X. Huang, X. Zhang, H.-Q. Yu, Photocatalytic degradation of atrazine by boron-doped TiO_2 with a tunable rutile/anatase ratio, Appl. Catal., B, 195 (2016) 69–76.
[30] J. Ma, J. Ding, L. Yu, L. Li, Y. Kong, S. Komarneni, BiOCl dispersed on NiFe-LDH leads to enhanced photo-degradation of Rhodamine B dye, Appl. Clay Sci., 109 (2015) 76–82.
[31] L. Jiang, K. Wang, X. Wu, G. Zhang, S. Yin, Amorphous bimetallic cobalt nickel sulfide cocatalysts for significantly boosting photocatalytic hydrogen evolution performance of graphitic carbon nitride: efficient interfacial charge transfer, ACS Appl. Mater. Interfaces, 11 (2019) 26898–26908.
[32] T. Fujii, F.M.F. de Groot, G.A. Sawatzky, F.C. Voogt, T. Hibma, K. Okada, *In situ* XPS analysis of various iron oxide films grown by NO_2-assisted molecular-beam epitaxy, Phys. Rev. B, 59 (1999) 3195–3202.
[33] Y. Li, C. Wang, H. Zheng, F. Wan, F. Yu, X. Zhang, Y. Liu, Surface oxygen vacancies on WO_3 contributed to enhanced photothermo-synergistic effect, Appl. Surf. Sci., 391 (2017) 654–661.
[34] Q. Hao, Z. Mo, Z. Chen, X. She, Y. Xu, Y. Song, H. Ji, X. Wu, S. Yuan, H. Xu, H. Li, 0D/2D Fe_2O_3 quantum dots/g-C_3N_4 for enhanced visible-light-driven photocatalysis, Colloid Surf., A, 541 (2018) 188–194.
[35] P.K. Malik, S.K. Saha, Oxidation of direct dyes with hydrogen peroxide using ferrous ion as catalyst, Sep. Purif. Technol., 31 (2003) 241–250.
[36] W. Li, Y. Wang, A. Irini, Effect of pH and H_2O_2 dosage on catechol oxidation in nano-Fe_3O_4 catalyzing UV-Fenton and identification of reactive oxygen species, Chem. Eng. J., 244 (2014) 1–8.
[37] G. Fan, X. Zheng, J. Luo, H. Peng, H. Lin, M. Bao, L. Hong, J. Zhou, Rapid synthesis of Ag/AgCl@ZIF-8 as a highly efficient photocatalyst for degradation of acetaminophen under visible light, Chem. Eng. J., 351 (2018) 782–790.
[38] G. Fan, Y. You, B. Wang, S. Wu, Z. Zhang, X. Zheng, M. Bao, J. Zhan, Inactivation of harmful cyanobacteria by Ag/AgCl@ZIF-8 coating under visible light: efficiency and its mechanisms, Appl. Catal., B, 256 (2019) 117866, doi: 10.1016/j.apcatb.2019.117866.
[39] J. Hou, R. Wei, X. Wu, M. Tahir, X. Wang, F.K. Butt, C. Cao, Lantern-like bismuth oxyiodide embedded typha-based carbon via *in situ* self-template and ion exchange–recrystallization for high-performance photocatalysis, Dalton Trans., 47 (2018) 6692–6701.
[40] Y. Zheng, Z. Yu, H. Ou, A.M. Asiri, Y. Chen, X. Wang, Black phosphorus and polymeric carbon nitride heterostructure for photoinduced molecular oxygen activation, Adv. Funct. Mater., 28 (2018) 1705407, doi: 10.1002/adfm.201705407.
[41] X.-W. Lei, C.-Y. Yue, J.-C. Wei, R.-Q. Li, F.-Q. Mi, Y. Li, L. Gao, Q.-X. Liu, Novel 3D semiconducting open-frameworks based on cuprous bromides with visible light driven photocatalytic properties, Chem. Eur. J., 23 (2017) 14547–14553.
[42] M. Chen, H. Xu, Q. Wang, D. Li, D. Xia, Activation mechanism of sodium percarbonate by FeOCl under visible-light-enhanced catalytic oxidation, Chem. Phys. Lett., 706 (2018) 415–420.
[43] R. Jiang, G. Lu, Z. Yan, D. Wu, R. Zhou, X. Bao, Insights into a CQD-$SnNb_2O_6$/BiOCl Z-scheme system for the degradation of benzocaine: influence factors, intermediate toxicity and photocatalytic mechanism, Chem. Eng. J., 374 (2019) 79–90.
[44] Y.-X. Yan, H. Yang, Z. Yi, T. Xian, R.-S. Li, X. Wang, Construction of Ag_2S@$CaTiO_3$ heterostructure photocatalysts for enhanced photocatalytic degradation of dyes, Desal. Water Treat., 170 (2019) 349–360.
[45] Y.-x. Yan, H. Yang, Z. Yi, X. Wang, R. Li, T. Xian, Evolution of Bi nanowires from BiOBr nanoplates through a $NaBH_4$ reduction method with enhanced photodegradation performance, Environ. Eng. Sci., 37 (2020) 64–77.
[46] J. Jiang, K. Zhao, X. Xiao, L. Zhang, Synthesis and facet-dependent photoreactivity of BiOCl single-crystalline nanosheets, J. Am. Chem. Soc., 134 (2012) 4473–4476.
[47] W. Ouyang, F. Teng, X. Fang, High performance BiOCl nanosheets/TiO_2 nanotube arrays heterojunction UV photodetector: the influences of self-induced inner electric fields in the BiOCl nanosheets, Adv. Funct. Mater., 28 (2018) 1707178, doi: 10.1002/adfm.201707178.
[48] W. Zhang, X.a. Dong, B. Jia, J. Zhong, Y. Sun, F. Dong, 2D BiOCl/$Bi_{12}O_{17}Cl_2$ nanojunction: enhanced visible light photocatalytic NO removal and *in situ* DRIFTS investigation, Appl. Surf. Sci., 430 (2018) 571–577.
[49] X. Yan, H. Zhao, T. Li, W. Zhang, Q. Liu, Y. Yuan, L. Huang, L. Yao, J. Yao, H. Su, Y. Su, J. Gu, D. Zhang, *In situ* synthesis of BiOCl nanosheets on three-dimensional hierarchical structures for efficient photocatalysis under visible light, Nanoscale, 11 (2019) 10203–10208.
[50] J. Li, C. Xiao, K. Wang, Y. Li, G.-K. Zhang, Enhanced generation of reactive oxygen species under visible light irradiation by adjusting the exposed facet of $FeWO_4$ nanosheets to activate oxalic acid for organic pollutant removal and Cr(VI) reduction, Environ. Sci. Technol., 53 (2019) 11023–11030.
[51] C. Xiao, J. Li, G.-K. Zhang, Synthesis of stable burger-like α-Fe_2O_3 catalysts: formation mechanism and excellent photo-Fenton catalytic performance, J. Cleaner Prod., 180 (2018) 550–559.
[52] T. Guo, K. Wang, G.-K. Zhang, X.-Y. Wu, A novel α-Fe_2O_3@g-C_3N_4 catalyst: synthesis derived from Fe-based MOF and its superior photo-Fenton performance, Appl. Surf. Sci., 469 (2019) 331–339.

Supporting information

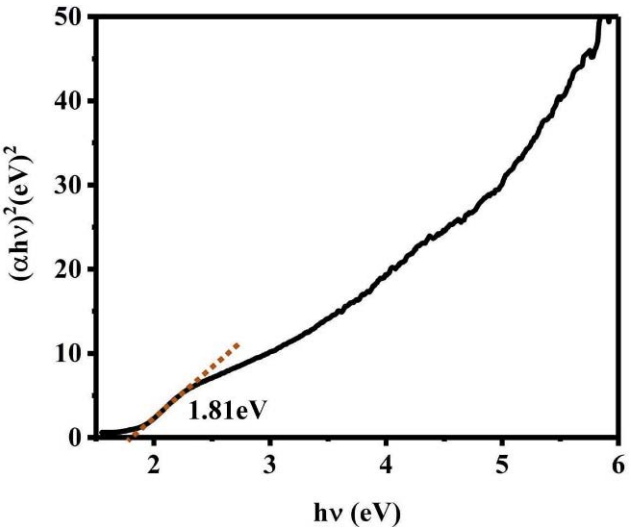

Fig. S1. Bandgap value of the pure FeOCl.

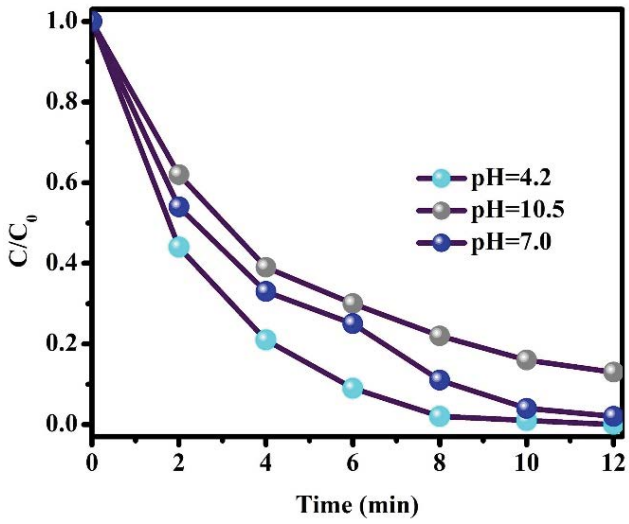

Fig. S3. Photo-Fenton catalytic activity of BiOCl/FeOCl-2 by different pH values.

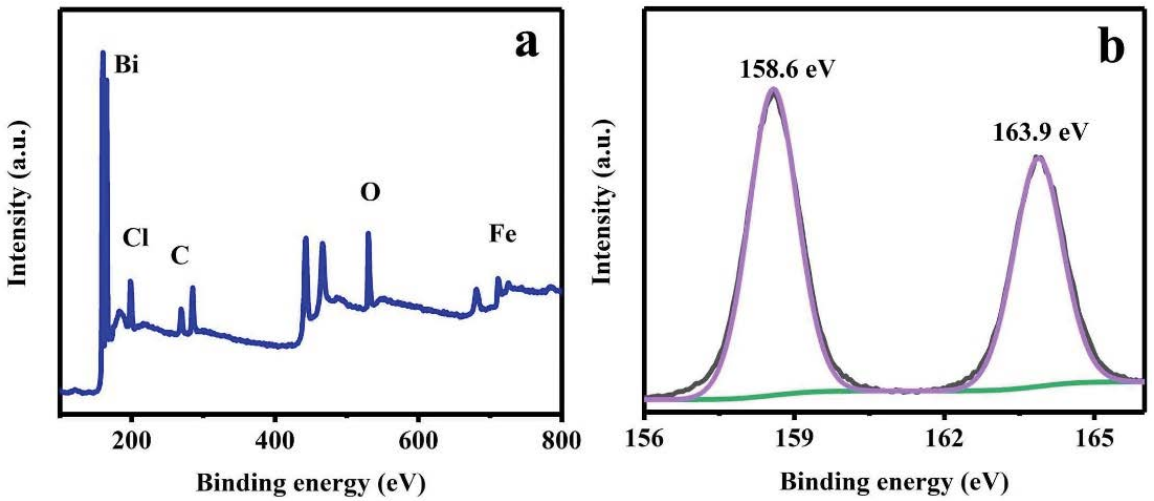

Fig. S2. XPS spectrums of (a) BiOCl/FeOCl-2, (b) Bi 4f XPS spectrums in BiOCl/FeOCl-3.

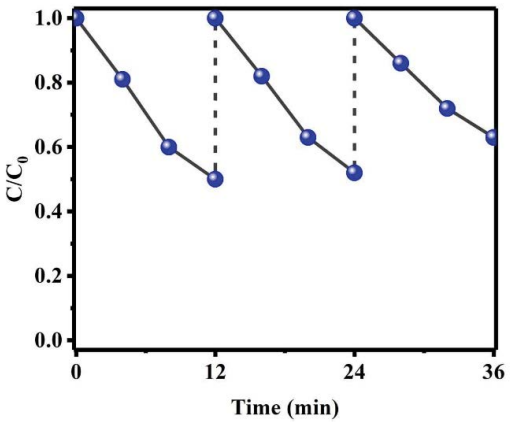

Fig. S4. Cycling experiments of pure FeOCl.

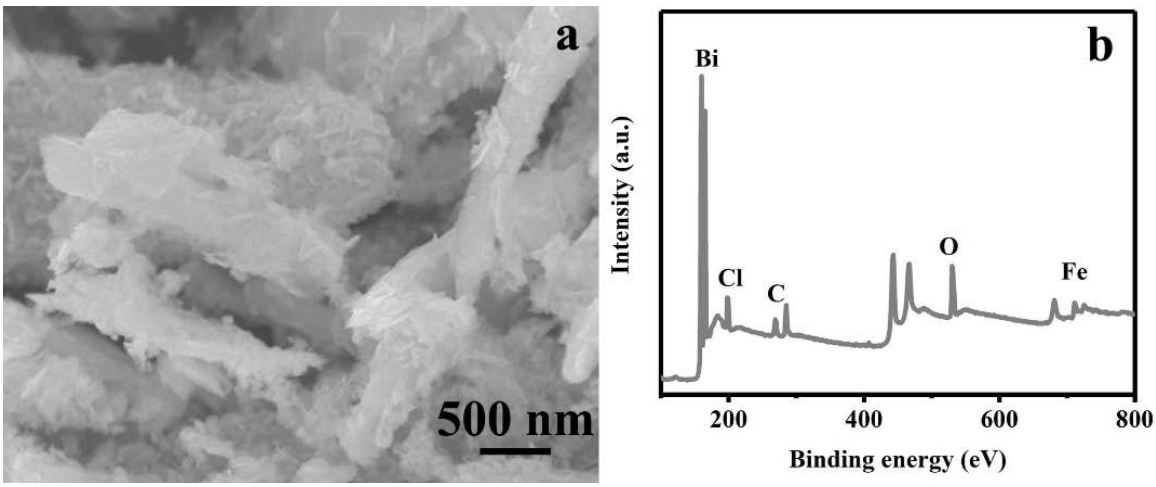

Fig. S5. (a) SEM image and (b) XPS spectrums of the BiOCl/FeOCl-2 after reaction.